Assessing RANS numerical and modelling properties in the simulation of the flow around fixed and moving cylinders

Rita Mendonça e Costa
ritamcosta@tecnico.ulisboa.pt

Instituto Superior Técnico, Universidade de Lisboa, Portugal

November 2019

Abstract

The analysis of the flow around bluff bodies is a well reviewed topic in computational fluid dynamics (CFD) since it provides a canonical test case to perform code verification and solution validation. Furthermore, it features complex physical phenomena (transition, separation, vortex shedding...) over a wide range of Reynolds numbers, whose study finds relevant applications in the fields of aeronautics and offshore renewable energies. This work focuses on the statistically unsteady flow around a circular cylinder, at a Reynolds number of 1×10^4, in fixed and imposed motion conditions. The Reynolds-averaged Navier-Stokes (RANS) equations are used for modelling in order to capture mean flow properties (in the sense of an ensemble average), and closed with the $k-\omega$ SST turbulence model. Two-dimensional test cases are studied. An analysis of the available moving/deforming grid techniques to handle imposed motion is performed, and the influence of the chosen technique on the selected set of boundary conditions for the computational domain is studied. A systematic procedure to calculate the statistical, iterative and discretization error is presented, both for the fixed and imposed motion cases, and a brief analysis of results from three dimensional simulations is performed. Finally, flow field details are evaluated for selected test cases, a validation exercise is presented, and the modelling limitations of the mathematical description are discussed. Similarities in the results obtained with the moving/deforming grid techniques are shown, and insight is provided on cases in which the RANS $+ k-\omega SST$ formulation successfully/unsuccessfully captures the mean flow properties.
Keywords: Cylinder, Moving/Deforming grids, RANS, Ensemble average, $k-\omega$ SST.

1. Introduction and Motivation

The analysis of the flow around cylinders employed in the supporting structures of offshore platforms has been an extensively documented topic in ocean engineering literature. Moreover, low aspect ratio cylinders (being this quantity defined as the ratio between the cylinder length, L, and the cylinder diameter, D), are known to model offshore platform support structures (e.g. spar, mono-column) more accurately than infinite/large aspect ratio cylinders. As for aeronautical applications, the study of the flow around bluff bodies has gained particular relevance in the noise-reduction studies performed for landing gears [1] and in the use of low aspect ratio circular pins as a "flow control means to mitigate separation over a flapped airfoil" [2].

1.1. Objectives

The core aim of the present work is to study the flow around fixed and moving cylinders (imposed periodical motion), in the latter case through the use of moving and deforming grid techniques, with different sets of boundary conditions applied. Additionally, since no clear agreement has been found in the available literature regarding the choice of **deforming/moving** grid methods to accurately simulate the movement, the present study aims at providing further insight on this topic, analysing the problem from a numerical standpoint and assessing the modelling error of the obtained results, taking as a reference the available experimental data from the literature. Furthermore, there is a focus in the analysis of some relevant flow features (such as the characterization of the vortical patterns in the cylinder wake) and in the discussion of the recorded differences between the 2D and 3D test cases. An additional objective is to diagnose relevant techniques allowing to identify if the Reynolds equations in a statistically unsteady problem (such as the moving cylinder) are capturing only the mean flow. If the diffusion provided by the turbulence model is not sufficient, there is a risk to start solving unwanted fluctuations.

2. Background

The three-dimensional analysis of the flow around cylinders has been a well-reviewed topic over time. Gonçalves [3] presented a comprehensive analysis of the flow around very low aspect ratio fixed cylinders. Additionally, the experimental work of Gonçalves [4] and numerical contributions of Rosetti et al. [5] shed additional light on the understanding of the flow around moving cylinders (both in free motion and imposed motion). In [5] a moving grid approach was used for the numerical treatment of the mesh used in the moving cylinder case.

2.1. Vortex shedding: flow regimes and synchronization regions for imposed motion

Williamson [6] collected a thorough historical perspective on the developments concerning the wake of bluff

bodies. In his work [6], an overview of vortex shedding regimes across a wide range of Reynolds numbers is presented. These range from the **laminar steady regime**, with a steady recirculation region comprising two symmetrical vortices on each side of the wake (for $Re < 49$), followed by the **laminar vortex shedding**, and subsequent **wake transition**, **shear layer transition** and **boundary layer transition**. The sequence of regimes is mainly motivated by fundamental shear flow instabilities (thoroughly detailed in [6]), whose description is beyond the scope of the current investigation. For $Re = 1 \times 10^4$ (Reynolds number of the present computations), the flow is, according to [6], in the **shear layer transition regime**. Additionally, Williamson [7] also characterized the several vortex synchronization regions in the cylinder wake as a function of the period/amplitude of the imposed motion, using as relevant parameters the **amplitude** and **wavelength** ratio (most commonly referred to as **reduced velocity**), defined as follows:

$$Amplitude\,ratio = \frac{A}{D} \tag{1}$$

$$Wavelength\,ratio\,(Reduced\,Velocity) = \frac{UT}{D} = \frac{\lambda}{D} \tag{2}$$

3. Problem Formulation

3.1. The RANS formulation for unsteady flows

When solving turbulent flows, it is often useful to adopt a Reynolds decomposition approach to deal with the intrinsically unsteady features of turbulence. The Reynolds decomposition can be applied to both steady and unsteady flows, being the only difference between the two the **definition of the mean value** of the decomposition: in **steady flows**, the mean value of the decomposition represents the **time average** of the quantity of interest, whereas in **unsteady flows**, the mean value of the decomposition represents the **ensemble average** of the quantity of interest. Thus, for an unsteady flow, the Reynolds decomposition is

$$\phi(x_i,t) = \overline{\phi}(x_i,t) + \phi'(x_i,t) \tag{3}$$

with

$$\overline{\phi}(x_i,t) = \lim_{N\to\infty} \frac{1}{N} \sum_{n=1}^{N} \phi(x_i,t) \tag{4}$$

Applying the averaging technique to the continuity and momentum equations, the following result is obtained (for incompressible flow), in tensor notation and Cartesian coordinates:

$$\frac{\partial(\rho\overline{u_i})}{\partial x_i} = 0 \tag{5}$$

$$\frac{\partial(\rho\overline{u_i})}{\partial t} + \frac{\partial}{\partial x_j}\left(\rho\overline{u_i}\,\overline{u_j} + \rho\overline{u_i'u_j'}\right) = -\frac{\partial\overline{p}}{\partial x_i} + \frac{\partial\overline{\tau_{ij}}}{\partial x_j} \tag{6}$$

The 2003 version of the $k-\omega$ SST model [8] is used in the present study in order to provide closure for the RANS equations.

3.2. Computational Domain

Bearing in mind an important goal of validating the numerical work developed in the present project, the experimental data of Gopalkrishnan [9] was taken as a reference for the choice of computational domain. As displayed in figure 1 (and taking the origin of the $x-y$ coordinate system to be placed at the center of the cylinder) the inlet of the rectangular domain was placed at $x = -40D$, the outlet at $x = +78D$ and the side walls at $y = +51D$ and $y = -51D$. The depth of the computational domain (along the z direction) was later adjusted according to the cylinder length used in the 3D test cases.

3.3. Boundary Conditions

One of the main goals was to select physically accurate BC in order to mimic the experimental conditions; additionally, it was fundamental to ensure compatibility between the chosen boundary conditions and the deforming/moving grids methods employed in the moving cylinder test cases. This second goal was found to be relevant after performing some tests and empirically verifying that an additional set of boundary conditions should be tested in order to seek a solution for the identified problem. This aspect is further explored in subsection 3.3.2.

3.3.1 First set of boundary conditions: BC-DEF

The following set of boundary conditions was selected (the corresponding names used in figure 1 are also presented):

- **Inlet:** uniform flow, with specified streamwise velocity vector ($\tilde{\mathbf{V}} = (\mathbf{1},\mathbf{0},\mathbf{0})[\mathbf{m/s}]$), specified k and ω, and pressure (p) extrapolated; ***(BCInflow)***

  From an inlet turbulence intensity $I = 1 \times 10^{-2}$, $k = 1.5\times10^{-4}U_\infty^2\,[m^2/s^2]$ is obtained. Furthermore, using $\frac{\nu_t}{\nu} = 1 \times 10^{-4}$, ω can be obtained from $\omega = \frac{k}{\nu_t}\,[1/s]$.

- **Outlet:** specified pressure ($p = 0$), and null streamwise derivatives for the remaining quantities ($\frac{\partial\phi}{\partial x} = 0$); ***(BCPressure)***

- **Top and bottom walls:** specified normal velocity component ($V_y = 0$) and null normal derivatives for the remaining quantities ($\frac{\partial\phi}{\partial y} = 0$); ***(BCSlipwall)***

- **Side walls:** symmetry condition, $V_z = 0$; ***(BCSymmetryPlane)***

- **Cylinder wall:** no-slip and impermeability boundary condition, with all velocity components set to be equal to the wall velocity, and the normal pressure derivative equal to zero. No wall functions were used. ***(BCWall)***

3.3.2 Second set of boundary conditions: BC-MVG

In the simulations concerning the use of a moving grid setup, the same choice of boundary conditions specified for the deforming grid were originally applied. Nevertheless, after performing the calculations according to this setup, artificial pressure oscillations were observed, which motivated a second choice of boundary conditions. Namely, at

the outlet surface, the streamwise derivatives of all dependent variables were set to zero ($\frac{\partial \phi}{\partial x} = 0$), corresponding to the ***BCOutflow*** designation in the software *ReFRESCO*. At the top and bottom walls the pressure was specified to be zero (in order to avoid free pressure values in the direction of motion of the cylinder), with null normal derivatives for the remaining quantities ($\frac{\partial \phi}{\partial y} = 0$), corresponding to the ***BCPressure*** designation. The remaining boundary conditions were maintained with respect to the BC-DEF setup. Figure 1 illustrates both the computational domain dimensions and the BC-DEF set of boundary conditions analysed.

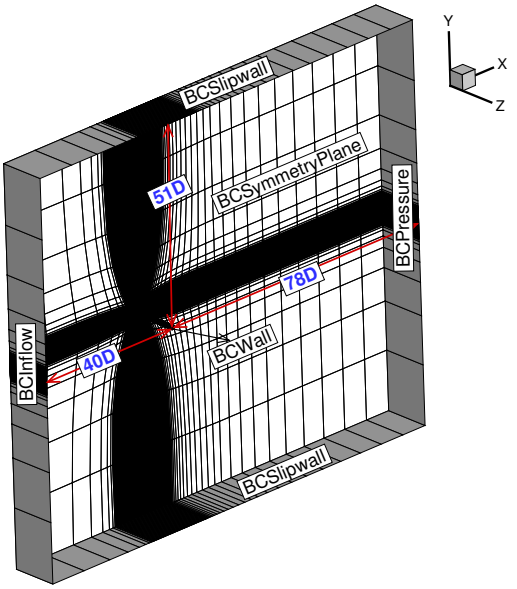

Figure 1: **BC-DEF** set of boundary conditions and computational domain dimensions.

4. Solution Procedure

4.1. Software *ReFRESCO*

The 2.5 version of the *ReFRESCO* software was used in all the computations performed in the present work. *ReFRESCO* is a viscous-flow CFD code that solves multiphase (unsteady) incompressible flows using the Navier-Stokes equations.

4.2. Numerical Model

The software *ReFRESCO* employs a PETSc (*Portable Extensible Toolkit for Scientific Computation*) solver for the linear equations, and for the mass-momentum coupling. The convective fluxes in the momentum equations were in the present work discretised using a LIMITED QUICK scheme [10] (QUICK scheme with a flux limiter), whereas for the turbulence equation a first order upwind (FOU) scheme was used. The time integration was performed using an implicit three-time level (2nd order) scheme for all equations, except for turbulence. In this case a first order scheme had to be employed, for robustness purposes.

4.3. Grids

The grids used in this investigation were obtained using the *Grid Generation Tools for Structured Grids* [11]. The structured grids generated for the simulations followed a multi-block approach, with different regions in the computational domain, in order to better capture the features of the flow. As displayed in figure 2, the grid is symmetric with respect to the x axis and therefore only the part of the grid with positive y coordinates is presented.

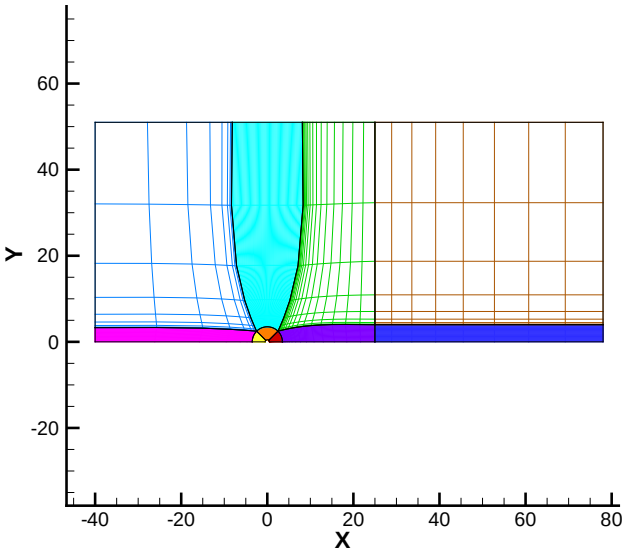

Figure 2: Details of the blocks used in the structured grid. Due to symmetry with respect to the x axis, only half of the whole computational domain is presented.

The grid blocks were designed in order to appropriately capture the near wall and near wake region of the cylinder. Consequently, a near-wall circular region (with a **3.5D** radius) was used, and the near wake region was extended to a length of **25D**. This strategy allowed a good capturing of the flow features in these zones (which comprised a greater number of grid points), without unnecessarily overloading the remaining blocks with a significant number of cells. In order to be able to later provide an estimation of the discretisation error (through a grid refinement study), several grids were generated, with a different number of points placed on the surface of the cylinder. Table 1 displays this information for all the used grids. The values indicated under the column "grid name" specify the number of points placed per each sector of 45 on the surface of the cylinder; therefore, the total number of points on the whole surface is obtained through a multiplication by 8.

Grid name	(h_i/h_1)	Points on the cylinder surface	Total elements
Grid 40	1.6	$40 \times 8 = 320$	18400
Grid 48	1.33	$48 \times 8 = 384$	26496
Grid 56	1.14	$56 \times 8 = 448$	36064
Grid 64	1.00	$64 \times 8 = 512$	47104
Grid 80	0.80	$80 \times 8 = 640$	73600
Grid 96	0.67	$96 \times 8 = 768$	105984
Grid 112	0.57	$112 \times 8 = 896$	144256

Table 1: Number of points used on the surface of the cylinder for each of the generated grids, and total number of elements in each of the grids.

4.4. Mesh deformation and moving mesh algorithms

A fundamental part of the present study focused on the use of two distinct deforming grid methods when performing

the moving cylinder calculations. The Delaunay Graph Mapping (DGM) method, [12] the Radial Basis Function (RBF) interpolation method and the Inverse Distance Weighting (IDW) interpolation method are examples of point-by-point techniques for mesh deformation. Both the RBF and IDW methods are used in the present work, and the underlying theory concerning these techniques can be found in [13] and [14]. Using a moving grid method is an alternative approach that can be used for the moving cylinder test case. It essentially consists in displacing the grid cells according to the imposed motion on the object, without enforcing fixed boundaries on the computational domain. This procedure was also employed in the present work, in order to provide additional data to be compared with the results obtained through the use of the two mesh deformation algorithms. It shall be recalled that the use of a moving grid approach implied/motivated the definition of a new set of boundary conditions, as previously explained in subsection 3.3.2.

4.5. Test Cases

All the cases evaluated in the course of the present investigation comprised **one** fixed or driven cylinder placed in the previously described computational domain, with the aforementioned (two) sets of boundary conditions, at a Reynolds number of $Re = 10,000$. The choice of this parameter followed the aim of backing up the numerical and experimental results of Rosetti et al. [5] and Gopalkrishnan [9], respectively. The driven motion test cases followed literature data found in [5] [9], and therefore a sinusoidal motion was imposed to the cylinder, $y(t) = Asin(\omega_i t)$, being $y(t)$ the transverse coordinate of the cylinder center over time, A the amplitude of the prescribed periodic motion and ω_i the dimensional frequency of the movement. Following [5] and [9], the non-dimensional amplitude $\mathbf{A/D = 0.3}$ was selected, and a range of reduced velocities (which specify the non-dimensional motion period) $\mathbf{U_R = UT_i/D}$ from 3 to 10 was chosen. Finally, additional three-dimensional driven motion test cases were included in order to provide a relevant comparison with the corresponding two-dimensional setups.

4.6. Quantities of interest

A few post-processing routines were written in *FORTRAN 90* in order to compute the minimum, maximum, average and *rms* values of the total force coefficients and perform a FFT (*Fast Fourier Transform*) of the forces' time series in order to evaluate the frequency content of the obtained signals (this was later used for the statistical convergence study, which will be further explored in section 5). For the sake of brevity, only the results concerning the CD_{avg} and the CL_{rms} will be detailed in the present document, since they were considered to be representative of the overall trends observed for the remaining computed quantities.

5. Numerical Convergence

5.1. General considerations

The main objective of the numerical convergence studies (developed in detail for the 2D cases) was the comparison of the fixed and forced motion test cases with respect to the behaviour of the numerical error. A fundamental aspect that had to be taken into account when performing the numerical convergence studies was the range of grids selected for each of the fixed and imposed motion cases. It was found that, in the imposed motion cases, the frequency content revealed by the time history of the forces was not as expected for all the generated grids. Therefore, before quantifying the statistical and iterative components of the error, an aspect that was found to deserve attention at an early stage was the analysis of the frequency content displayed by the time traces of the force coefficients. Thus, a **FFT** *(Fast Fourier Transform)* analysis was performed for the solutions obtained for all the grids, in order to evaluate if significant differences were found in the frequency spectrum. Figures 3 and 4 display the obtained FFT for two of the test cases. A clear peak is identified in the fixed case, corresponding to the natural frequency associated with the vortex shedding phenomenon. In the imposed motion case the first peak (also associated with the natural vortex shedding) is also present, displaying however a slight shift in frequency relatively to the fixed case. The second peak (with greater intensity) represents the excitation frequency of the imposed motion ($f = 1/U_R$). When refining the grid - from **grid 64** to **grid 80** - it was observed that the frequency content displayed by the FFT changed. While for the fixed the case the difference was minimal (slight broadening of the energy peak corresponding to the natural vortex shedding phenomenon, figure 3), the imposed motion case revealed the appearance of unwanted low frequency content in the signal (figure 4). This was confirmed by an analysis of the time history of the force coefficients, which showed the appearance of additional low frequencies, both in moving and deforming grid setups.

In order to analyse if the selected timestep for the simulations was appropriate, a test was performed for $U_R = 5.0$, (for all the grids), using both a constant $\Delta t_i/\Delta t_1$ and a constant h_i/h_1. Figure 5 displays the result for the variable CD_{avg}. The influence of changing the grid refinement ratio is preponderant over the influence of changing $\Delta t_i/\Delta t_1$, which justifies the use of a constant Courant number for the grid/time refinement studies.

Naturally, the appearance of low frequency fluctuations with grid/time refinement questions if the mean flow properties - according to the selected RANS formulation - are correctly being captured. Thus, only the cases that displayed well defined energy peaks - predictably representing in fact the mean flow frequency content - in the corresponding FFT were selected for the statistical and iterative convergence studies. Table 2 identifies the grids for which the obtained frequency spectrum was as expected, both for the fixed and imposed motion setups.

Reduced velocity (U_R)	Grids with expected frequency content
< 3	None
3	40, 48, 56, 64
5	40, 48, 56, 64
10	40, 48, 56, 64, 80
∞ (Fixed case)	40, 48, 56, 64, 80, 96

Table 2: Grids used for the numerical error estimation in the fixed and imposed motion test cases.

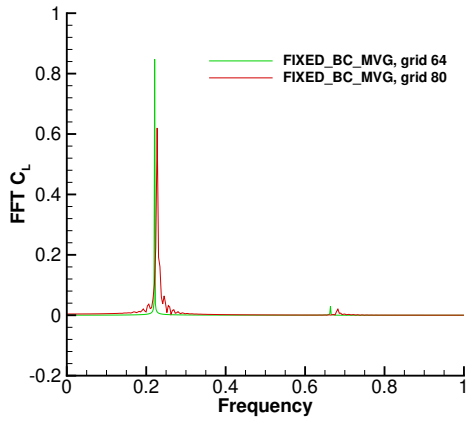

Figure 3: Frequency content of the C_L signal, for the fixed case, (FIXED-BC-MVG setup), using an iterative tolerance of 5×10^{-6}. Result obtained for **grid 64** and **grid 80**.

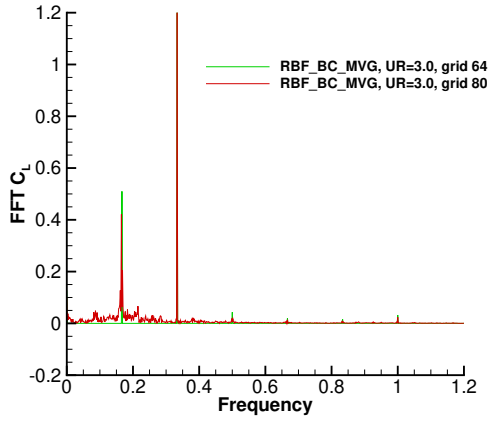

Figure 4: Frequency content of the C_L signal, for the reduced velocity $U_R = 3.0$, (RBF-BC-MVG setup), using an iterative tolerance of 5×10^{-6}. Result obtained for **grid 64** and **grid 80**.

5.2. Statistical convergence studies

The plots presented in figures 6 and 7 display the evolution of the percentage statistical error (computed according to the methodology proposed by Brouwer in [15]), for the variable CD_{avg} and for both the 2D fixed cases and 2D imposed motion cases (with $U_R = 3.0$). The behaviour of the variable CL_{rms} was found to be quite similar and is herein omitted for the sake of brevity.

The first aspect that stands out when analysing figures 6 and 7 is the difference in the evolution of the statistical error in the fixed vs. imposed motion case. On the one hand, it is clear that in the fixed case, the statistical error reaches a *plateau* for values of iterative tolerance lower than 1×10^{-5} (approximately). On the other hand, for the imposed motion scenario, the statistical error displays a steady decreasing trend as the iterative tolerance is lowered. Furthermore, it is relevant to compare the order of magnitude of the statistical error for both cases, for typical values chosen for the iterative tolerance; establishing this comparison for 5×10^{-4}, it is clear that the statistical

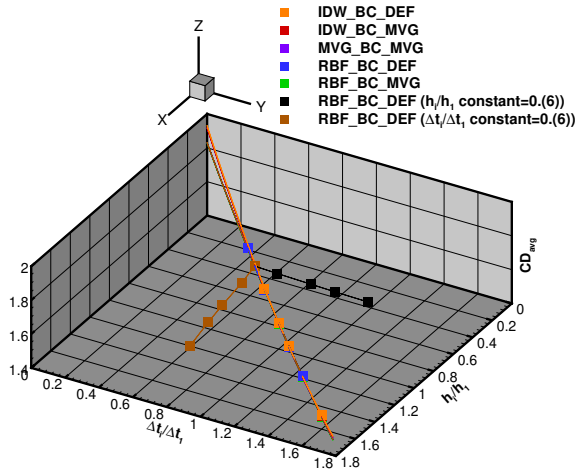

Figure 5: CD_{avg} for all the imposed motion setups, $U_R = 5.0$, with $\Delta t_i/\Delta t_1 = h_i/h_1$, with constant $\Delta t_i/\Delta t_1 = 0.(6)$ and constant $h_i/h_1 = 0.(6)$.

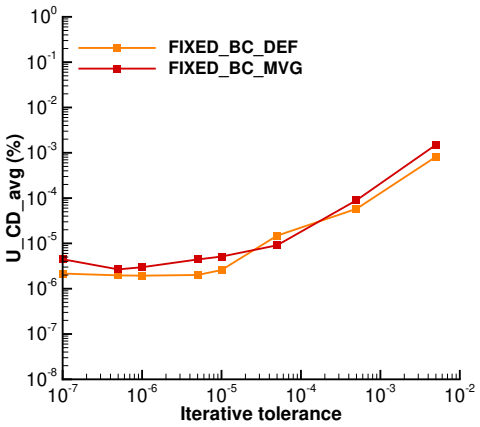

Figure 6: Statistical uncertainty for CD_{avg} as a function of iterative tolerance, for the **fixed case**.

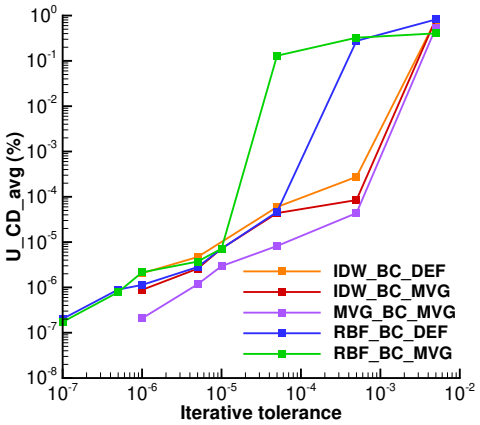

Figure 7: Statistical uncertainty for CD_{avg} as a function of iterative tolerance, for the **imposed motion** case with $U_R = 3.0$.

error is unacceptably large in the imposed motion scenario ($\approx 1 \times 10^{-1}$ to 1×10^{0} for the RBF method), while low

enough in the fixed cases (lower than 1×10^{-3} for the selected variable).

5.3. Iterative convergence studies

The iterative error associated to the selected variables (for the same test cases) was also evaluated, using the procedure referenced in [16] to perform error estimation. Figure 8 displays the iterative convergence behaviour for the CD_{avg} in the imposed motion setups with $U_R = 3.0$, for the reference grid (grid 64). The results for the fixed test cases and for CL_{rms} are herein omitted for the sake of brevity. After this analysis, an iterative tolerance of $\mathbf{5 \times 10^{-6}}$ was chosen for the remaining test cases (run over a total of **200** cycles).

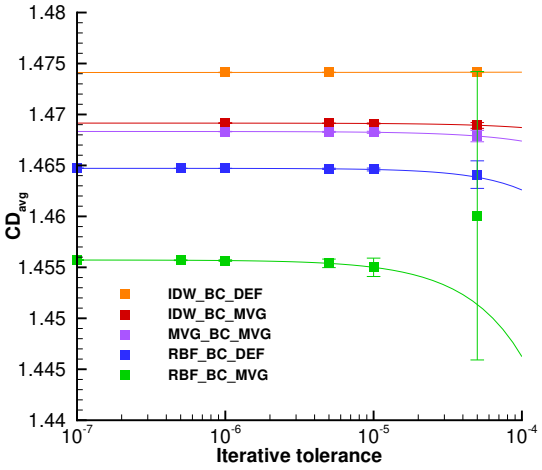

Figure 8: Iterative convergence for CD_{avg} for the **imposed motion** case with $U_R = 3.0$.

5.4. Grid/time refinement studies

The reference procedures found in [17] were used to perform the discretisation error estimation. It shall be outlined that the grid refinement ratio and time refinement ratio were maintained from grid to grid, in order to preserve the initial CFL condition tuned for the reference grid. That is,

$$\frac{h_i}{h_j} = \frac{\Delta t_i}{\Delta t_j} \tag{7}$$

being the subscripts i and j used in the present case to designate any subset of two grids i, j from the set of four grids initially selected. The grid refinement studies were carried out for the fixed and imposed motion cases (with all three reduced velocities). However, the results for $U_R = 10.0$ are herein omitted as they approach the ones obtained with the fixed setup.

5.4.1 2D Fixed cylinder

Figure 9 displays the grid refinement study performed for the fixed case, with and without including the two finest grids tested in this case (grids 80 and 96). The improvement in the convergence behaviour is clear in both setups, with the addition of the two finest grids. This trend displays the ideal situation that would be desirable in the imposed motion cases - that is, the use of two additional, finer grids - if not for the shortcomings concerning the appearance/resolution of unwanted frequencies with grid refinement (as previously explained for the case of $U_R = 3.0$). Figure 9 shows both setups on the same plot.

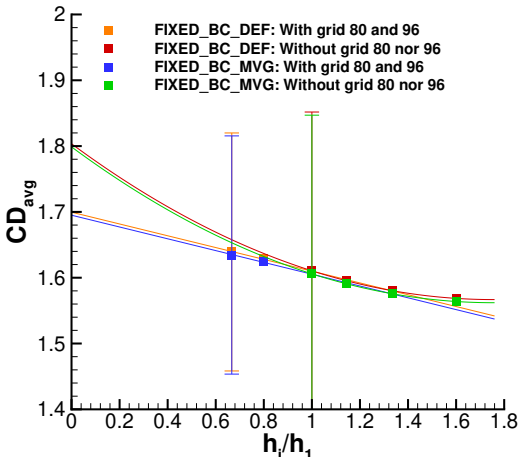

Figure 9: Convergence behaviour for both setups (FIXED-BC-DEF and FIXED-BC-MVG), superimposed on the same plot.

5.4.2 2D Moving cylinder: $U_R = 3.0$

Grid number	Number of timesteps per cycle	Δt [s]
40	100	0.03
48	120	0.025
56	140	0.0214(285714)
64	160	0.01875

Table 3: $U_R = 3.0$: selected grids and corresponding Δt for the grid refinement study

Figure 10 displays the trend observed in the computed CD_{avg} when adding the information corresponding to grids 80, 96 and 112 (for which the FFT of the time history of the force coefficients revealed unwanted low frequency oscillations, as previously mentioned). As it is clearly seen, the data points corresponding to these grids are completely off-trend with respect to the remaining grids (and there is even a clear difference between the RBF-BC-DEF and RBF-BC-MVG setups for grid 80, outlined with black circles), which is a good indication that, in this case, the mean flow properties are not correctly captured anymore, leading to a mathematical model that depends on the grid size, which is not the goal of RANS.

5.4.3 2D Moving cylinder: $U_R = 5.0$

Figure 11 displays the curve fit for the four selected grids in this case (identified in table 4), along with the data points corresponding to the simulations using grid 80, for the IDW-BC-DEF setup, and grids 80, 96, and 112 for

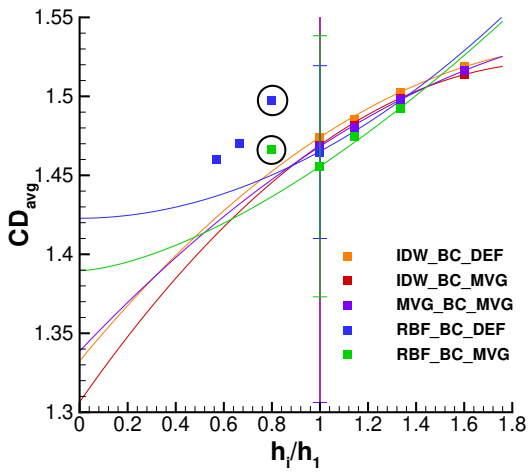

Figure 10: Grid refinement study for CD_{avg}, for $U_R = 3.0$, using the four selected grids, **with the addition of grid 80** (for the RBF-BC-MVG setup) and **grids 80, 96 and 112** (for the RBF-BC-DEF setup).

Grid number	Number of timesteps per cycle	Δt [s]
40	125	0.04
48	150	0.0(3)
56	175	0.0(285714)
64	200	0.025

Table 4: $U_R = 5.0$: selected grids and corresponding Δt for the grid refinement study

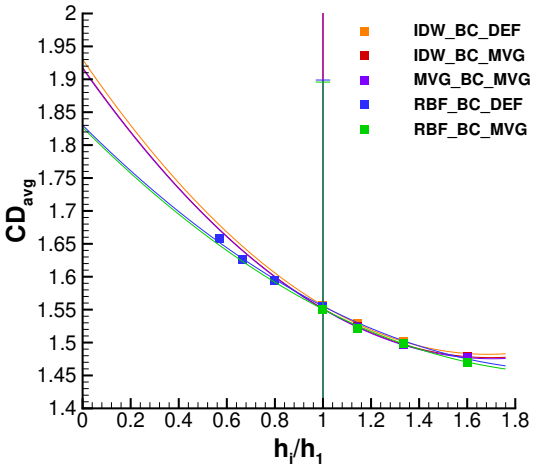

Figure 11: Grid refinement study for CD_{avg}, for $U_R = 5.0$, using the four selected grids, **with the addition of grid 80** for the IDW-BC-DEF setup and **grids 80, 96 and 112** for the RBF-BC-DEF setup.

the RBF-BC-DEF setup. In this case, it was observed that the appearance of undesired frequency content in the time traces of the force coefficients did not significantly affect the convergence behavioural trend (the data points corresponding to grid 80 for the IDW-BC-DEF and RBF-BC-DEF setups are even superimposed, due to a very negligible difference in the CD_{avg} value), possibly due to the fact that in the lock-in region, in which the vortex shedding frequency and the external excitation frequency collapse onto one, the expected frequency content is still well separated from the low frequency oscillations appearing with grid refinement. However, no error estimation was performed for the three finest grids, since it was still not entirely clear if the mean flow properties were accurately being captured.

5.5. 3D Analysis

The analysed 3D test cases used the RBF-BC-DEF setup, and three different cylinder aspect ratios were evaluated: $L/D = 3.0; 6.0; 12.0$. Figure 12 shows the influence of the cylinder aspect ratio in the frequency spectrum of the lift coefficient signal. Reducing the length from $L/D = 12.0$ to 6.0 (and even further to 3.0) leads to the appearance/growth of the low frequency energy peaks in the response, which confirms the decrease of the dissipation provided by the turbulence model as the cylinder aspect ratio (length) is decreased. Finally, figures 13 and 14 display the data points obtained for the two variables of interest (CD_{avg} and CL_{rms}), for grids 40, 48, and 56. In the 3D cases, the unwanted frequency content is even more significant than in the 2D simulations; therefore, the systematic procedure to compute statistical variables of interest employed in the 2D study is no longer applicable in the present case (which is revealed by the differences in the calculated variables when using the last 40 or 100 cycles of the time history of the forces, as shown in figures 13 and 14 for L/D = 3.0) and the obtained force coefficients should be evaluated under a conservative point of view. All in all, the results obtained display the clear shortcomings of a RANS formulation (already identified in the 2D cases) in the studied 3D cases: the appearance of well distributed low frequency content questions the correct attainment of mean flow properties, due to a lack of diffusion provided by the employed turbulence model to filter these frequencies.

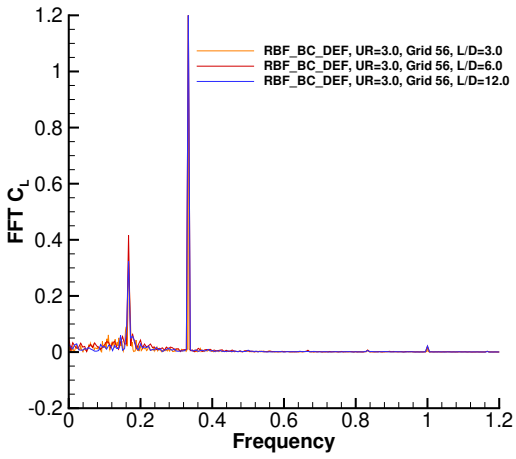

Figure 12: FFT analysis for the lift coefficient signal, using the RBF-BC-DEF setup, $U_R = 3.0$, **grid 56**, for $L/D = 3.0$, 6.0, and $L/D = 12.0$.

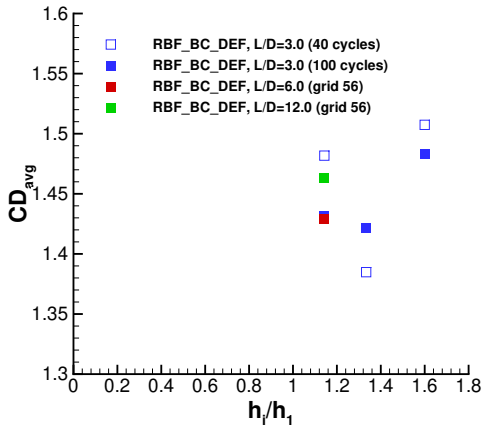

Figure 13: Data points for CD_{avg}, for $U_R = 3.0$ and $L/D = 3.0$, RBF-BC-DEF setup (grids 56, 48, 40). Additional points for $L/D = 6.0$ and $L/D = 12.0$ displayed for **grid 56**.

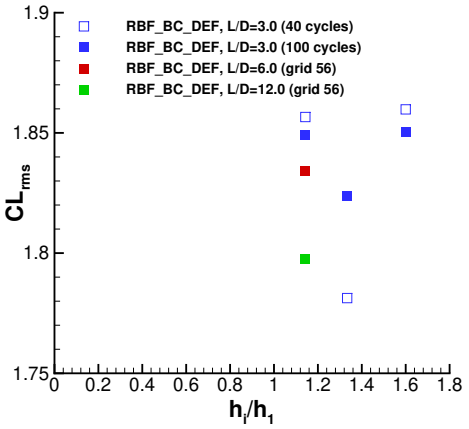

Figure 14: Data points for CL_{rms}, for $U_R = 3.0$ and $L/D = 3.0$, RBF-BC-DEF setup (grids 56, 48, 40). Additional points for $L/D = 6.0$ and $L/D = 12.0$ displayed for **grid 56**.

6. Comparison with experimental data and flow analysis

6.1. Validation exercise: 2D and 3D cases

Figure 15 presents the collection of 2D imposed motion results (with an additional data point at $U_R = 3.2$), the reference experimental data from Gopalkrishnan [9] and the 3D imposed motion results obtained. The information displayed concerns the average drag coefficient (CD_{avg}), a representative parameter for this analysis. The proximity of the 2D numerical results to the experimental data is clear for $U_R = 3.0$; however, this matching between results appears to be progressively lost as the reduced velocity is increased (that is, the experimental data is still comprised within the numerical error bars for $U_R = 5.0$, in spite of some difference in the results, and for $U_R = 10.0$ the numerical and experimental data are clearly different). Additionally, the proximity of the 2D results and experimental data for the lowest reduced velocity, $U_R = 3.0$ (that is, the greatest frequency of excitation) suggests that the three-dimensional effects become less and less relevant for

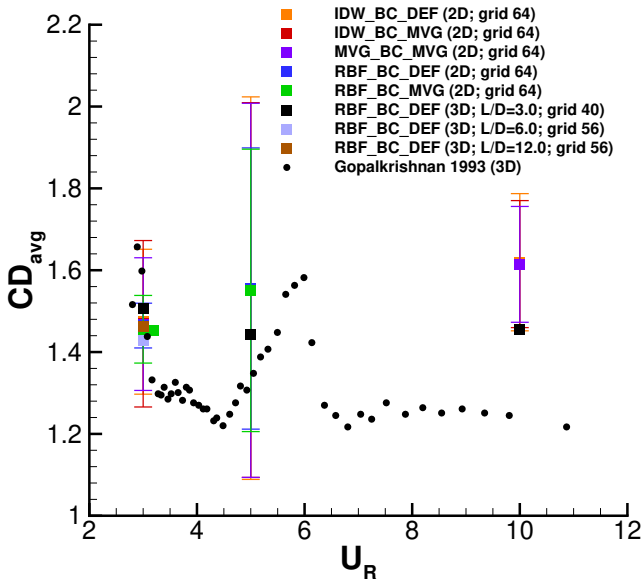

Figure 15: Comparison of the obtained 2D and 3D numerical results (for all setups) with the available experimental data (3D) for the selected range of reduced velocities (U_R), adding the point corresponding to $U_R = 3.2$.

situations in which the cylinder is moving with a greater externally imposed frequency (situations in which the inertial terms are preponderant in the overall momentum balance, in comparison to the diffusive terms). On the other hand, as U_R is increased (that is, as the frequency of excitation is decreased and the cylinder approaches a fixed condition, which would correspond to $U_R = \infty$), the differences between the 2D and 3D cases become extremely clear. The proximity of the data point corresponding to $U_R = 3.2$ to the points corresponding to $U_R = 3.0$ reinforces the confidence in the matching with the experimental data, in this range of reduced velocities. Furthermore, the 3D numerical results comply with the previously presented hypothesis: in fact, it is clear that there is a small difference between the 2D/3D cases for the lowest reduced velocity ($U_R = 3.0$), whereas this difference becomes more apparent as the reduced velocity increases. Thus, in spite of the identified problems for $U_R = 3.0$ with respect to capturing the mean flow, this case is also the one in which the 2D/3D/experimental have a better match, which confirms that, as the reduced velocity is decreased, the role of diffusion/turbulence modelling also decreases with respect to the overall momentum balance.

6.2. Vortex synchronization regions along the reduced velocity spectrum (2D cases)

The main characteristics of the cylinder near-wake were compared for all three reduced velocities ($U_R = 3.0$, 5.0 and 10.0), taking as a reference the work of Williamson [7], in which the vortex synchronization regions in the cylinder near wake were characterized. Furthermore, a comparison was also established for the different combinations deform-

ing/moving grid methods + set of BC used in the present work. Only the results obtained for $U_R = 3.0$ are herein presented.

6.2.1 Near wake for $U_R = 3.0$

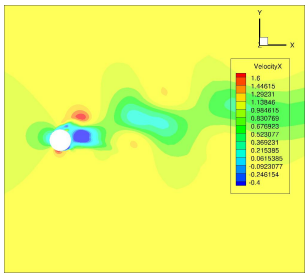

Figure 16: Instantaneous x velocity plot for the **RBF-BC-DEF** setup, at point of minimum lift coefficient, for $U_R = 3.0$.

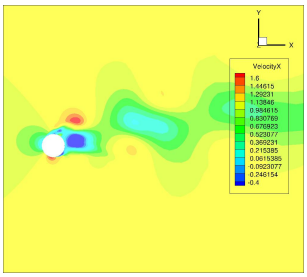

Figure 17: Instantaneous x velocity plot for the **MVG-BC-MVG** setup, at point of minimum lift coefficient, for $U_R = 3.0$.

Figures 16 and 17 display the coalescence pattern identified by Williamson in [7] (C mode), in which the small structures coalesce in the cylinder's nearest wake. Furthermore, in spite of the selected set of BC and moving/deforming grid setup chosen, the well known near wake structures are correctly captured in both cases, and match the vortex synchronization patterns identified by Williamson in his work [7].

6.3. Modelling limitations of a RANS formulation in statistically unsteady flows

As stated by Pereira in [18], the success of using a RANS formulation will naturally depend on the "ability of the closure strategy to represent the flow field". That is, the RANS approach will essentially be appropriate when the largest, energy containing scales of turbulence are accurately modelled. For the practical case of this study - a statistically unsteady flow - this would imply a good separation (in terms of the frequency spectrum) between the mean flow and the turbulent structures. However, as it has been shown along this analysis, the presence of coherent structures (such as the vortex shedding phenomenon) essentially poses a possible interaction with turbulent structures, then making the "analysis of flow-fields non-trivial", as observed by Pereira in [18]. All in all, the aforementioned aspects support the narrow range of application of a RANS formulation in statistically unsteady flows - confirmed by the numerical simulations run in the course of the present work - and pose the need to accurately define this range with precise indicators.

6.4. Indicators to evaluate the suitability of the RANS approach

The **effective Reynolds number** (defined as follows), and previously proposed by Pereira [18] is a relevant indicator to evaluate this suitability:

$$Re_{eff} = \frac{U_\infty D}{\nu + \nu_t} = Re \frac{1}{1 + \frac{\nu_t}{\nu}} \tag{8}$$

As stated by Pereira in [18], "an effect of modelling a fraction of the turbulence field is the reduction of the effective Reynolds number at which the computations are performed". Hence, a qualitative indicator of how appropriate the mathematical modelling is (meaning that only the mean flow is captured and turbulence is entirely modeled) will be the extension of regions in which a low effective Reynolds number is observed (specifically, lower than 1000, which corresponds to the onset of the shear layer transition regime identified by Williamson in [6]) in the cylinder near wake. The analysis of the effective Reynolds number plots displayed (expectable) differences in the onset of the shear layer transition regime found for all three imposed motion cases ($U_R = 3.0, 5.0, 10.0$). The figures are herein omitted for the sake of brevity. Naturally, due to a difference in the external excitation frequency, the region corresponding to an effective Reynolds number lower than 1000 will be different in each of the three cases. However, after identifying this region in all cases (say, for reference grid 64), it is possible to evaluate how the effective Reynolds number changes in the near wake when the grid is refined.

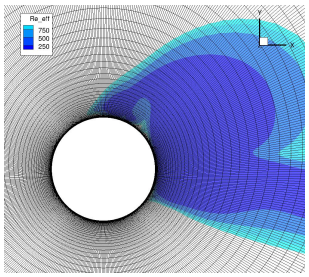

Figure 18: Effective Reynolds number in the cylinder near wake, at the point of minimum lift coefficient, **for grid 64**, using the RBF-BC-DEF setup at a reduced velocity $U_R = 3.0$.

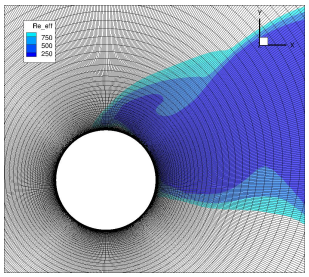

Figure 19: Effective Reynolds number in the cylinder near wake, at the point of minimum lift coefficient, **for grid 80**, using the RBF-BC-DEF setup at a reduced velocity $U_R = 3.0$.

Figures 18 and 19 display this comparison. It is visible that the extension of the region with $Re_{eff} < 1000$ clearly decreases when refining the grid (from grid 64 to grid 80), which reinforces the thesis that the turbulence model used for closure is not efficiently damping out turbulent fluctuations, leading to an undesired resolution (instead of modelling) of turbulent scales. The use of this indicator reveals a viable strategy to qualitatively assess the suitability of the chosen modelling approach. Moreover, the monitoring of local variables (velocity, pressure) that was carried out at given points on the cylinder near wake showed the appearance of unwanted frequency content with grid refinement, which strengthens the analysis carried out so far and sheds additional light on RANS modelling properties in statistically unsteady flows.

7. Conclusions

An extensive comparison of the results obtained with both sets of boundary conditions (BC-DEF and BC-MVG)

and with the deforming/moving grid techniques was performed, both for the fixed and imposed motion scenarios. Overall, it was found that the influence of the chosen BC and moving/deforming grid technique on the computed solution was negligible. Additionally, comparable results were registered for the near wake vortex synchronization patterns, as seen in chapter 6).

One the most important findings yielded by this analysis concerns the behaviour of the frequency content in both fixed and imposed motion scenarios with respect to grid refinement. The appearance of unwanted low frequencies was predominant for the lowest reduced velocities (namely, $U_R = 3.0$), becoming less relevant for the fixed and highest reduced velocity cases. This behaviour was attributed to a particularly strong lack of diffusion in the former cases, which essentially caused an undesired resolution of turbulent scales by the model, preventing an appropriate capturing of the mean flow properties and ultimately questioning the validity of a RANS formulation complemented with a $k - \omega SST$ turbulence model in these cases. The effective Reynolds number, along with the FFT from the force coefficients' signals, proved to be valuable tools to identify the test cases in which the mean flow properties were successfully captured.

7.1. Future Work

As for the identification/development of relevant sensors to provide a stronger assessment of the RANS formulation modelling properties, the work of Pereira [18] has already presented successful contributions concerning this aspect. In order to extend the already developed analysis, the use of the effective Reynolds number (computed with local velocity, instead of the reference velocity, U_∞), could yield additional information to provide a better distinction between the cases with different reduced velocities. Additionally, a technique to identify the relative importance of convective/diffusive terms in the overall momentum balance could be developed, thus quantifying the contribution of diffusion from the turbulence model in each test case. And finally, assessing the behaviour of a different turbulence model (instead of the herein used $k - \omega$ SST) could be a useful pathway for additional insight on this specific topic.

References

[1] Taro Imamura, Tohru Hirai, Kazuhisa Amemiya, Yuzuru Yokokawa, Shunji Enomoto, and Kazuomi Yamamoto. Aerodynamic and Aeroacoustic Simulations of a Two-wheel Landing Gear. volume 1, pages 293–302. IUTAM Symposium on Computational Aero-Acoustics for Aircraft Noise Prediction, 2010. doi:10.1016/j.proeng.2010.09.031.

[2] Samantha Gildersleeve, Dan Clingman, and Michael Amitay. Flow around Low Aspect Ratio Cylinders and their Applications for Flow Control. AIAA 2017-1449, Grapevine, Texas, AIAA SciTech Forum, 55th AIAA Aerospace Sciences Meeting 2017. doi:10.2514/6.2017-1449.

[3] R. T. Gonçalves, G. R. Franzini, G. F. Rosetti, J. R. Meneghini, and A. L. C. Fujarra. Flow around circular cylinders with very low aspect ratio. *Journal of Fluids and Structures*, 54:122–141, 2015. doi:10.1016/j.jfluidstructs.2014.11.003.

[4] R. T. Gonçalves, J. R. Meneghini, and A. L. C. Fujarra. Vortex-induced vibration of floating circular cylinders with very low aspect ratio. *Ocean Engineering*, 154:234–251, 2018. doi:10.1016/j.oceaneng.2018.02.019.

[5] G. F. Rosetti and G. Vaz. On the numerical simulations of captive, driven and freely moving cylinder. *Journal of Fluids and Structures*, (74):492–519, August 2017. doi:10.1016/j.jfluidstructs.2017.06.013.

[6] C. H. K. Williamson. *Vortex dynamics in the cylinder wake*. Mechanical and Aerospace Engineering, Upson Hall, Cornell University, 1996.

[7] C. H. K. Williamson and A. Roshko. Vortex formation in the wake of an oscillating cylinder. *Journal of Fluids and Structures*, 2:355–381, January 1988. doi:10.1016/S0889-9746(88)90058-8.

[8] F. R. Menter, M. Kuntz, and R. Langtry. Ten years of Industrial Experience with the SST Turbulence Model. *Turbulence, Heat and Mass Transfer*, 4, 2003. Begell House, Inc.

[9] Ramnarayan Gopalkrishnan. *Vortex-Induced Forces on Oscillating Bluff Cylinders*. Doctoral dissertation, Woods Hole Oceanographic Institution Massachusetts Institute of Technology, Woods Hole, Massachusetts 02543, February 1993. WHOI-92-38.

[10] *ReFRESCO controls documentation*. version 2.5.0.

[11] Luís Eça. Grid Generation Tools for Structured Grids. Technical report, MARIN/IST cooperative research project, may 2003.

[12] Pieter Coulier and Eric Darve. Efficient mesh deformation based on radial basis function interpolation by means of the inverse fast multipole method. *Computer methods in applied mechanics and engineering*, (308):286–309, June 2016. doi:10.1016/j.cma.2016.05.029.

[13] J. Windt. Incompressible Flow Simulations on Moving and Deforming Grids - Part II: Mesh Deformation. Final Report 70058-2-RD, ARD Maritime Research Institute Netherlands, Haagsteg 2 6708 PM Wageningen The Netherlands, September 2013. ARD 2013.

[14] J. Windt. Improvement of the Grid Deformation Methods in ReFRESCO. Final Report 70058-7-RD, ARD Maritime Research Institute Netherlands, Haagsteg 2 6708 PM Wageningen The Netherlands, January 2015. ARD 2014.

[15] J. Brouwer, J. Tukker, and M. van Rijsbergen. Uncertainty Analysis of Finite Length Measurement Signals. pages 260–274, Gdansk, Poland, 2013. 3rd International Conference on Advanced Model Measurement Technology for the EU Maritime Industry (AMT'13).

[16] Luís Eça, G. Vaz, S. L. Toxopeus, and M. Hoekstra. Numerical Errors in Unsteady Flow Simulations. *Journal of Verification, Validation and Uncertainty Quantification*, 4, June 2019. doi:10.1115/1.4043975.

[17] L. Eça and M. Hoekstra. A procedure for the estimation of the numerical uncertainty of CFD calculations based on grid refinement studies. *Journal of Computational Physics*, 262:104–130, January 2014. doi:10.1016/j.jcp.2014.01.006.

[18] Filipe Miguel Soares Pereira. *Towards Predictive Scale-Resolving Simulations of Turbulent External Flows*. Phd degree in computational engineering, Instituto Superior Técnico, 2018.